PCCP

PAPER

View Article Online
View Journal

Cite this: DOI: 10.1039/c4cp01898b

Interplay of chemical structure and magnetic order coupling at the interface between Cr_2O_3 and Fe_3O_4 in hybrid nanocomposites†

Ruth Otero-Lorenzo,[a] Mads C. Weber,[bc] Pamela A. Thomas,[d] Jens Kreisel[bc] and Verónica Salgueiriño*[a]

Received 2nd May 2014,
Accepted 14th August 2014

DOI: 10.1039/c4cp01898b

www.rsc.org/pccp

Hybrid nanocomposites based on ferrimagnetic (FiM) Fe_3O_4 and magnetoelectric antiferromagnetic (AFM) Cr_2O_3 nanocrystals were synthesized to offer a particular three-dimensional (3D) interface between the two oxides. This interface favours an intermixing process (demonstrated by combining Raman spectroscopy and magnetization measurements) that determines the final magnetic behavior.

Introduction

Heterostructures of transition metal oxides can offer particularly interesting interfaces by downsizing the nanocrystals forming them. This interface is characterized by an energetic change that cannot be nullified but reduced by local relaxation related to processes of diffusion and chemical ion redistribution.[1] The correlation between chemical composition and structure considering the particularities of the nanoscale systems, taking into account ion and vacancy diffusion lengths, becomes therefore an important dynamical variable to control the final properties of nanostructures characterized by the interface, for example, in nanocomposites. For example, changes in the cationic valence state associated with changes in the oxygen vacancy concentration profoundly affect magnetic, electronic and transport properties.[2] Accordingly, developments in the synthetic approaches to exploit and control the different mobilities of cations and anions to engineer gradients in static and dynamic chemistry and carrier concentrations will be very convenient.[3]

Beberwyck *et al.* recently highlighted postsynthetic modifications of preformed nanostructures for the construction of complex nanomaterials exploiting cation exchange reactions.[4] The interfaces established in this way offer a combination of effects depending on the local chemical composition, the crystallographic orientation, the type of coupling, and/or the 3D connectivity pattern between the transition metal oxide nanocrystals. As a result, the heterostructures allow therefore enhanced and/or diversified capabilities,[5] depending on the lattice, electronic and orbital reconstruction at the interfaces.[6] For that reason, the complete characterization of hybrid nanocomposites requires a combination of techniques such that the contributions from individual components and the density of the interfaces established can be uniquely described.

Herein, we report nanoparticulated composites based on ferrimagnetic (FiM) (and multiferroic at low temperatures) Fe_3O_4 and magnetoelectric and antiferromagnetic (AFM) Cr_2O_3. The particular three-dimensional (3D) interface established between the nanoparticles of the two oxides favours an intermixing process, which determines the interplay between chemical structure and magnetism.

Experimental section

Chromium oxide nanoparticles were synthesized by means of a controlled precipitation of $Cr(OH)_3$ in basic medium.[7] Accordingly, 5 mL of $Cr(NO_3)_3$ (0.1 M (Aldrich)) is added dropwise under mechanical stirring to 5 mL of NaOH (0.3 M (Aldrich)). Once the nanoparticles are formed, they are centrifuged, washed and annealed at 800 °C in air to promote the formation of the chromium oxide. Fe_3O_4–Cr_2O_3 nanocomposite synthesis was carried out by modification of a previous method reported to produce Fe_3O_4 nanoclusters.[8] $FeCl_3$ (5 mmol (Fluka)) was dissolved in ethylene glycol (40 mL (Aldrich)), followed by addition of NaAc

[a] Departamento de Física Aplicada, Universidade de Vigo, 36310 Vigo, Spain. E-mail: vsalgue@uvigo.es
[b] Département Sciences et Analyses des Matériaux, CRP Gabriel Lippmann, 4422 Belvaux, Luxembourg
[c] University of Luxembourg, 1511 Luxembourg, Luxembourg
[d] Department of Physics, University of Warwick, Gibbet Hill Road, Coventry, CV4 7AL, UK

† Electronic supplementary information (ESI) available: Fig. S1. Raman spectra of the hybrid nanostructures as a dried powder in the sample holder, collected at room temperature and in three different spots of the sample using the 633 nm excitation wavelength. Fig. S2 and S3 include the Raman spectrum of Cr_2O_3 nanoparticles and Fe_3O_4 nanocomposites, respectively. Fig. S4 includes a comparison of *M vs. H* hysteresis loops of nanocomposites of magnetite with and without chromium oxide. Fig. S5 includes the temperature dependent magnetization (collected under ZFC-FC conditions) of the nanocomposites. See DOI: 10.1039/c4cp01898b

(3.6 g (Aldrich)) and polyethylene glycol (1.0 g (Aldrich)), in the presence of the Cr_2O_3 (0.76 mg) nanoparticles previously synthesized. The mixture was stirred for 30 min and sealed in a Teflon lined stainless-steel autoclave, heated to and maintained at 185 °C for 8 h, and then allowed to cool down. The obtained black products were washed and dried.

The samples were characterized by transmission electron microscopy (TEM), performed on a JEOL JEM1010 instrument operating at an acceleration voltage of 100 kV. High resolution (HR) and high-angle annular dark-field scanning TEM (HAADF-STEM) and energy dispersive X-ray elemental analyses (EDS) were carried out on a field emission JEOL JEM2010F working at 200 kV. Samples for TEM and HRTEM analyses were prepared by dropping a diluted suspension of the nanocomposites onto an ultrathin carbon coated copper grid. X-ray diffraction patterns were collected using a Siemens D-5000 powder X-ray diffractometer (Cu K_α radiation (λ = 1.54056 Å) in the 10–90° 2θ range) and compared with crystallographic information files (CIF) from the crystallographic open database (COD). Raman spectra were collected using a Renishaw inVia Reflex Raman microscope. Experiments were conducted at room temperature using three different excitation wavelengths: a red 633 nm line from a HeNe laser, a green 514 nm line from an Argon laser and a blue 442 nm line from a HeCd laser with a spectral cut-off of at about 120 cm^{-1}. Magnetic measurements were performed using a Quantum Design MPMS XL7 SQUID magnetometer.

Results and discussion

The hybrid nanocomposites were synthesized using a solvothermal method in which the reaction mechanism is described as a two-stage growth process in which the primary nanocrystals of Fe_3O_4 nucleate first and then aggregate uniformly into larger secondary structures,[8] though in this case, in the presence of Cr_2O_3 nanoparticles previously synthesized.[7] The method offers increased amounts of the nanocomposites, implying therefore advantages in terms of low-cost production and up-scaling possibilities. The characterization of the as-synthesized heterostructures was performed with focus on the size, crystallinity and composition. Fig. 1a shows the Fe_3O_4–Cr_2O_3 nanocomposites, with an average diameter of 172 ± 24 nm (Gaussian analysis). HR-TEM (Fig. 1b) resolves the individual smaller units forming the composites, and HAADF-STEM in combination with STEM-XEDS elemental mapping shown in Fig. 1c and d demonstrates the hybrid morphology. Fig. 1c reflects the relative distribution of the metallic elements, with red and green areas corresponding to Cr and Fe, respectively, and underlines the random distribution of the two oxides forming the heterostructures. The Cr_2O_3 nanoparticles (~35 wt%) in the final composites have an average diameter of 51 ± 16 nm; Fe_3O_4 units (~65 wt%) are smaller with an average diameter of ~10 nm. Since the TEM images shown do not allow distinguishing the individual Fe_3O_4 nanoparticles, we have considered dark-field STEM images for their size distribution analysis.

The X-ray diffraction (XRD) pattern of the Fe_3O_4–Cr_2O_3 composites (in black), along with the reference patterns of

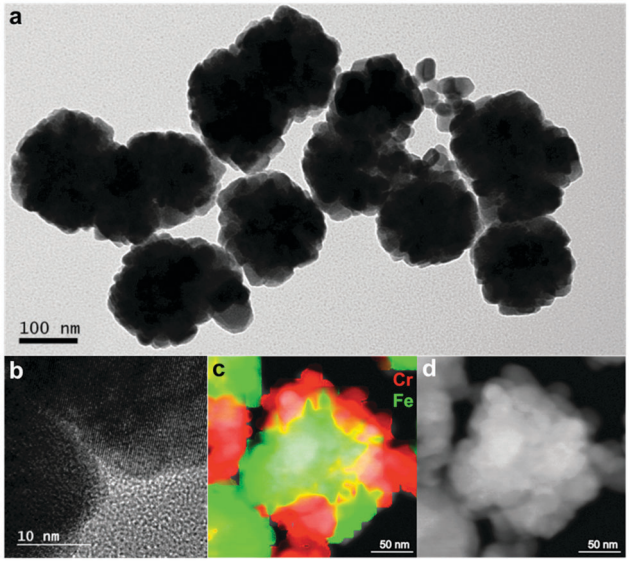

Fig. 1 TEM (a), HRTEM (b) and HAADF-STEM images (c and d) and EDS elemental mappings (in c) showing the distribution of the Cr (red) and Fe (green) within the nanocomposites.

magnetite (Fe_3O_4, green, ref.: JPCDS-ICDD card 10-0319) and eskolaite (Cr_2O_3, red, ref.: JPCDS-ICDD card 38-1479), are given in Fig. 2. Even though the units forming the composites are rather small (down to ~10 nm in the case of Fe_3O_4) and randomly orientated, as checked by TEM, it is possible to resolve the diffraction pattern. A comparison of the diffraction pattern of the composites to the references illustrates that it corresponds to the sample with Cr_2O_3 and Fe_3O_4 as main components and enables us to assign the intensities to diffracting planes of both oxides. The direct contact between oxides implies gradients of chemical potential that promote intermixing processes, favoring the formation of the mixed chromium–iron oxides such as $Cr_{2-x}Fe_xO_3$ and $Fe(Fe_{2-x}Cr_x)O_4$, considering the flow of Cr^{3+} ions to the magnetite phase and the flow of Fe^{3+} ions to the eskolaite phase. Indeed, kinetic

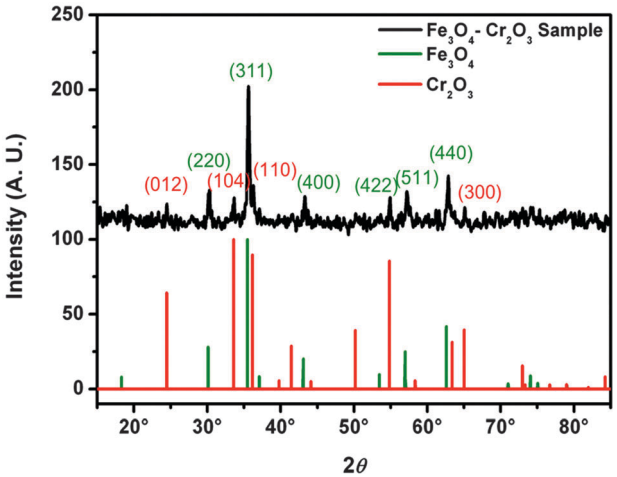

Fig. 2 XRD pattern of the Fe_3O_4–Cr_2O_3 sample (black) compared to reference patterns of magnetite (green) and eskolaite (red).

factors become key in determining the feasibility of an ion exchange reaction, especially at the nanoscale at which limits of long-range solid-state ion diffusion are significantly relaxed by the large surface-to-volume ratios.[4] The composites indeed present such a situation, which becomes rather favored considering the morphology attained by the heterostructures with the 3D connectivity pattern between both oxides. We can, however, disregard the formation of a mixed ferrite ($CrFe_2O_4$) considering a redox process to obtain Cr^{2+} from Cr^{3+} and Fe^{3+} from Fe^{2+} ions, given the standard reduction potentials.

Raman spectroscopy is a powerful probe for investigating vibrational and structural properties of materials[9] and can provide unique information for analyzing hybrid structures that combine several transition metal oxides. However, the power from a laser excitation source can lead to local heating in Raman experiments in transition metal oxides, especially when the laser beam is focused on a small spot size.[10–12] Taking this into account, we have carefully checked (for the three wavelengths employed) not to heat the sample in order to avoid modifications of the spectral signature. Additionally, considering the fact of studying hybrid nanocomposites, we have first verified the reproducibility of spectra on different places of the sample. Fig. S1 (ESI†) includes the Raman spectra of the sample containing the hybrid nanostructures as dried powder, collected at room temperature and in three different spots. The consistency of the different spectra obtained using a 1 μm laser spot reflects the homogeneity of the sample on a micrometer scale.

Though already routinely applied to thin films, Raman spectroscopy is less (but increasingly) used to characterize heterostructured and/or nanoparticulate-based materials.[13–16] Furthermore, the vast majority of Raman studies on oxides uses a single wavelength only, which is selected according to the best Raman signal or to reduce the substrate background signal and fluorescence. Here, we have employed different laser wavelengths for the investigation of the hybrid nanostructures, to allow differentiating the singular parts of the nanocomposites. Fig. 3a shows room temperature Raman spectra obtained for three different excitation wavelengths (442, 514 and 633 nm). The spectra consist of both broad features (for example, between 580 cm^{-1} and 760 cm^{-1} or between 260 cm^{-1} and 420 cm^{-1}, due to overlapping bands) and rather defined bands like the modes at 550 cm^{-1} or at 675 cm^{-1} when excited with the red laser. Although the spectra of different wavelengths are similar at first sight, a closer inspection reveals that the spectra present different features for different wavelengths. For understanding such dissimilar features three different but linked factors shall be considered; (a) the optical confocal depth, which decreases with a decrease in the wavelength for a given material, (b) absorption, since a decrease in the laser wavelength can lead to an increase in absorption and consequently reduction of the penetration depth, and (c) Raman cross section, the Raman intensity of a given material depending on the exciting wavelength can lead to resonant Raman effects.[13]

In order to assign the different spectral features of the hybrid nanocomposites in Fig. 3a, we discuss their different signatures by comparing the spectra to data from the literature for the

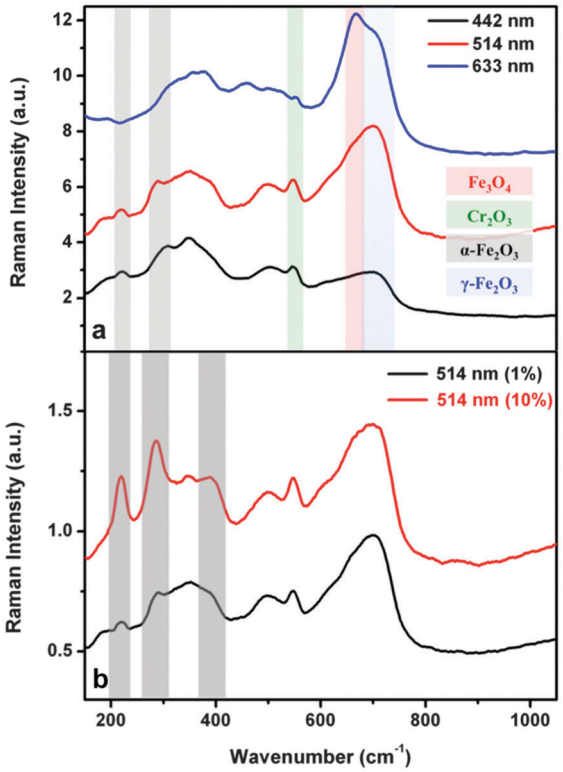

Fig. 3 (a) Comparison of the Raman spectra from the Fe_3O_4–Cr_2O_3 heterostructures obtained at different excitation wavelengths (442, 514 and 633 nm). (b) Comparison of the Raman spectra obtained using different densities of power (at 1 and 10%) from the laser excitation source (514 nm).

oxides the nanocomposites consist of, the main compounds being eskolaite (Cr_2O_3) and magnetite (Fe_3O_4).[10,16–20] We also take into account the spectra of the Cr_2O_3 nanoparticles previously synthesized and later used to include in the nanocomposites and of Fe_3O_4 nanocomposites (synthesized following the same method as the one herein reported, but in the absence of the chromium oxide nanoparticles) (see Fig. S2 and S3 in the ESI†). Additionally, we have to consider the mixed oxides mentioned before ($Cr_{2-x}Fe_xO_3$ and $Fe(Fe_{2-x}Cr_x)O_4$) as well as the possible formation of hematite (α-Fe_2O_3) and maghemite (γ-Fe_2O_3), especially at the interface between nanoparticles and at the surface of the outer nanoparticles in the composites (where an oxidation process is more favored).

Let us first recall the main features of the spectral signatures of potentially present materials. Fe_3O_4 crystallizes in the *Fd3m* space group which gives rise to five Raman active modes $\Gamma = A_g + E_g + 3T_{2g}$. Seven Raman active modes, $\Gamma = 2A_{1g} + 5E_g$, have been predicted by group theory for the $R\bar{3}c$ crystal structure of Cr_2O_3 as well as for the potentially formed α-Fe_2O_3. All possible modes have been observed in single crystal Raman spectroscopy measurements and reported by Hart *et al.* including mode assignment to the appropriate vibration symmetry.[17–19] In the case of Fe_3O_4, the main features appear at 675 cm^{-1} (A_{1g}) and 550 cm^{-1} (T_{2g}), though the A_{1g} mode is by far stronger than the T_{2g} mode. The Raman spectrum of Cr_2O_3 is dominated by a very intense mode A_{1g} at 553 cm^{-1} (see Fig. S2 and S3 in the ESI†).

The bands of the highest intensity of α-Fe_2O_3 can be found in the rather low energy region at around 230 cm^{-1} (A_{1g}), 253 cm^{-1} (E_g), 298 cm^{-1} (E_g + E_g). The spectrum of γ-Fe_2O_3 on the other hand shows rather broad features between 300 cm^{-1} and 400 cm^{-1}, 425 cm^{-1} and 540 cm^{-1} as well as between 600 cm^{-1} and 750 cm^{-1}.[10] Main mode bands appear marked in pale pink (Fe_3O_4), in pale green (Cr_2O_3), in pale blue (γ-Fe_2O_3), and in pale grey areas (α-Fe_2O_3) in the graphs in Fig. 3.

Having considered these most dominant features, all spectra show broad bands in the regions of 350 cm^{-1}, 500 cm^{-1} and 700 cm^{-1}, which reflect spectral signatures of maghemite (γ-Fe_2O_3) though the asymmetric shape and the high intensity of the feature between 580 cm^{-1} and 760 cm^{-1} suggests that this region cannot be explained only by the presence of this iron oxide. McCarty and Boehme reported a study on $Cr_{2-x}Fe_xO_3$ and $Fe(Fe_{2-x}Cr_x)O_4$ solid solutions.[20] The main feature of both solid solution systems was found in the region of 600 cm^{-1} and 720 cm^{-1} with an asymmetric deformation towards smaller wavenumbers due to several close bands and accordingly, the solid solutions of the iron and chromium oxides strongly contribute to the feature located at around 700 cm^{-1}. On the other hand we can appreciate that the excitation with the red laser leads to a change in the shape of this feature, when compared with spectra under excitation of the blue and green lasers, now dominated by a rather sharp band at around 675 cm^{-1}, which can be assigned to the strongest band in Fe_3O_4. Another well-defined band peaks at 550 cm^{-1} where both Fe_3O_4 and Cr_2O_3 have a vibration mode. This band is visible in all the spectra of different laser wavelengths whereas the band at 675 cm^{-1} of Fe_3O_4, which is the most dominant band of Fe_3O_4, can only be detected under excitation with the 633 nm laser. Therefore we assign the feature at 550 cm^{-1} as one of the A_{1g} modes of the Cr_2O_3 component of the nanocomposites. The observed changes in the intensity of the Raman spectra under excitation of different wavelengths, which enable especially the identification of the Cr_2O_3 and Fe_3O_4 phases, are due to different electronic structures and thus different resonant and absorption effects of these oxides. We note that the presence of mixed iron–chromium oxides as well as potential contributions from binary oxides is not surprising as they are expected to form the interface of Fe_3O_4 and Cr_2O_3. On the other hand, after such investigation with well-controlled laser power, we have also intentionally used higher laser power to test the effect of heating on our nanocomposites (Fig. 3b). Significant modifications, namely an intensity enhancement at around 220, 300 and 400 cm^{-1}, suggest a markedly increased proportion of α-Fe_2O_3.[10,12] However, a detailed investigation of this heating induced transformation and the likely impact on the coupling properties is beyond the scope of this publication.

The magnetic properties of the hybrid nanocomposites were recorded using a superconducting quantum interference device (SQUID) magnetometer at different temperatures and were examined in terms of magnetization, coercivity and exchange bias. The *M vs. H* curves (Fig. 4a and b) of the sample display open hysteresis loops in all the temperatures considered, even at 295 K. Instead of the typical superparamagnetic behavior

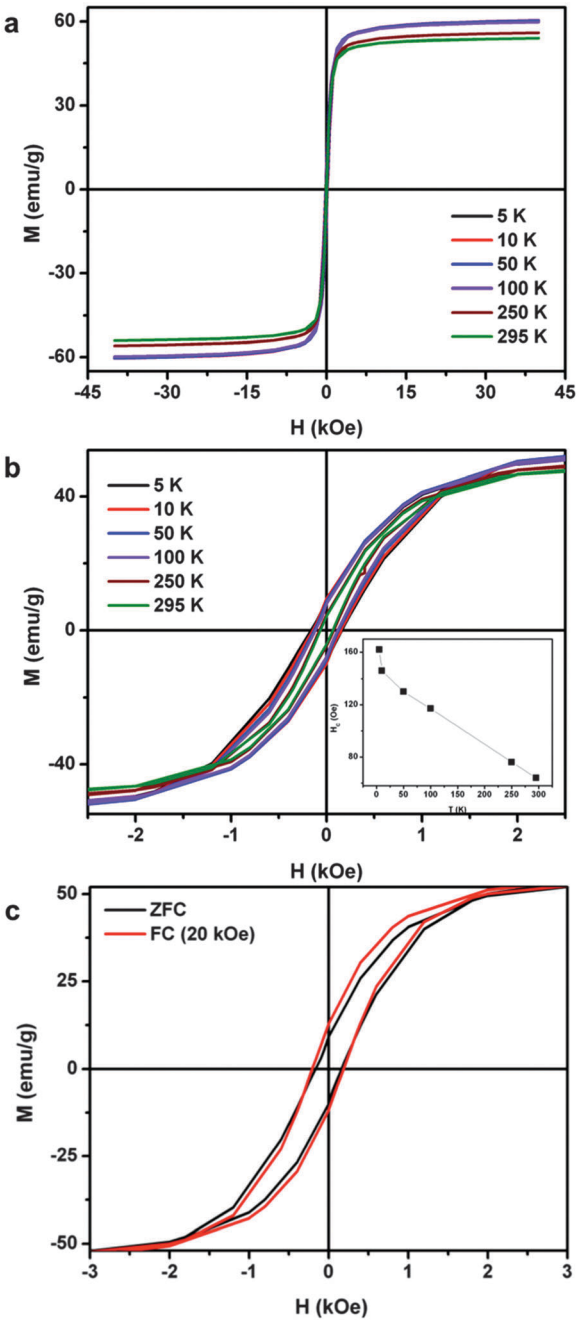

Fig. 4 Hysteresis loops of the hybrid nanocomposites recorded at different temperatures (a), hysteresis loops at low fields (b) and hysteresis loops at 5 K after zero-field cooling and field-cooling (20 kOe) (c).

expected for the Fe_3O_4 and Cr_2O_3 nanoparticles with close hysteresis loops, we can observe a blocked-like state due to the important interactions established in the sample, due to nanoparticle and nanocomposite interactions. Independent of their different magnetic orders, the FiM magnetite and the AFM Cr_2O_3 nanoparticles are expected to present a superparamagnetic behavior. In the case of the ~10 nm Fe_3O_4 nanoparticles, all the atomic magnetic moments become coupled to coherently fluctuate at room temperature as a one large nanoparticle magnetic moment.[21] In the case of Cr_2O_3,

since it is AFM, we have to consider only the atomic magnetic moments from the surface giving a paramagnetic contribution. Indeed, nanoparticles of AFM materials have non-zero magnetic moments and are therefore, strictly speaking, not AFM.[22–25] Numerous magnetization studies of AFM nanoparticles have shown that both the initial susceptibility and the magnetization in large applied fields are considerably larger than in the corresponding bulk materials. Néel justified this result due to the finite number of magnetic atoms in the nanoparticles, which may lead to a difference in the numbers of spins in the two sublattices because of the random occupancy of lattice sites.[26] This results in an uncompensated magnetic moment μ, which in the case of AFM nanostructures without impurities either of FM or FiM materials, comes from a random occupation of surface sites. On the other hand, the magnetoelectric AFM materials, like Cr_2O_3, have an equilibrium boundary polarization, which is coupled to the bulk AFM order parameter. This boundary polarization, roughness insensitive, has been demonstrated to contribute to the magnetization.[27,28]

Accordingly, the hysteresis loops included in Fig. 4 can be associated with these two main contributions; one responsible for the large magnetization values due to the ferrimagnetic (FiM) magnetite nanoparticles, which superimposes the antiferromagnetic contribution responsible for the subtle slope and almost non-saturation of the magnetization at high field values that corresponds to the chromium oxide magnetic phase identified. Fig. S4 (in the ESI†) includes the hysteresis loops collected at 10 K of two samples of magnetite nanocomposites (normalized on the graph on the right), synthesized in the absence and presence of Cr_2O_3 nanoparticles. From these graphs, it is clear that the magnetite-based sample reaches larger values of magnetization at much lower magnetic fields. The sample with the two oxides, the Fe_3O_4–Cr_2O_3 nanocomposites, shows lower values of magnetization and needs larger applied magnetic fields (due to the AFM chromium oxide). At 10 K (as shown in this graph in Fig. S4 (ESI†)), the magnetite-based sample reaches a M_S = 80 emu g^{-1} ($\sim$80% of the M_S value measured by Smit and Wijn for bulk[29]). In contrast the Fe_3O_4–Cr_2O_3 nanocomposites, because of the AFM chromium oxide, reaches a M_S = 60 emu g^{-1}.

The configuration or disposition of the nanoparticles, randomly assembled and coupled in the nanocomposites justifies the non-zero values of coercivity up to room temperature (see the inset in Fig. 4b). Fig. S5 (in the ESI†) shows the ZFC-FC (zero field cooled-field cooled) measurements, which in view of the morphology of the nanocomposites, reflect the important dipolar and exchange interactions between the units forming them. Accordingly, the irreversibility between the ZFC and FC curves appears shifted to high temperatures ($T_{irrev} > 290$ K), which agrees with the fact that the nanoparticles in the nanocomposites appear in a blocked-like state, and consequently, have non-zero though small values of coercivity, despite the relatively large average diameter of the nanocomposites. Therefore, the nanocomposite magnetic response depends directly, not only on the type of magnetic material formed, but also on the size of the nanoparticles and interactions established in between, and also influenced by the processes occurring at the 3D interface.

In this regard, we can also consider the coupling between the two magnetic orders, FiM and AFM, by means of an exchange bias (EB) effect. This effect leads to an extra anisotropy contribution, such that the effective magnetic anisotropy energy of the composites can become larger than the thermal energy. In such a situation, the total magnetic moments of the hybrid nanocomposites are prevented from flipping over the energy barrier for all temperatures below T_N (Cr_2O_3) = 310 K, and thus the composites remain magnetically stable below this temperature. On the other hand, we must note down the fact that nanoparticles of the same material, grouped in nanocomposites, can also be magnetically stable in the same range of temperatures.[30] Accordingly, the system was cooled with no field applied (ZFC) and under an applied magnetic field (FC) of magnitude H_{FC} = 20 kOe. Fig. 4c shows the hysteresis curves collected at 5 K (zero-field cooled (ZFC) and FC (20 kOe)) displaying a very small shift along the direction of the cooling field with coercivities $H_C = |H_{C1} - H_{C2}|/2$ = 163 Oe (ZFC) and H_C = 198 Oe (FC) and the exchange bias field $H_E = (H_{C1} + H_{C2})/2$ = 17 Oe (in the FC curve). The increase in coercivity and the small value of the exchange bias field H_E associated with the EB effect indicate uniaxial and unidirectional exchange anisotropies due to the exchange interaction between the uncompensated surface spins of Cr_2O_3 and Fe_3O_4 in the nanocomposites.[31] The interfacial interaction between the magnetite and chromium oxide appears to be the main source of exchange bias, taking into account the exchange interaction that gives rise to magnetic order in the metal oxides. This interaction is often mediated through adjacent oxygen atoms and has a strong indirect exchange component that tends to favour an AFM alignment of the spins. Additionally, a second option can consider a spin-glass, given the nanoparticulated morphology of the nanocomposites.[32] On the other hand, though clear that there is an exchange interaction between the two oxides, not only because of the shift of the hysteresis loop after field cooling, but also because of the increase in coercivity, we can point out two main reasons for the very low value of the exchange bias field H_E. First we can consider the fact of having a 3D interface between the two oxides, which averages out the exchange coupling and consequently the value of H_E, and second, we also have to take into account the postsynthetic metallic cation exchange at the interface between the two oxides, which can also decrease the value of H_E. Additionally, Fallarino *et al.* pointed out a limit in the magnetoelectric nature of the AFM Cr_2O_3 as the size decreases. As approaching this limit, the surface (boundary) magnetization can even dominate the magnetic response of otherwise antiferromagnetically ordered nanoparticles,[33] which can therefore minimize the AFM–FiM interaction required for the EB effect to happen.

Conclusions

In summary, we have presented a combination of techniques to characterize hybrid nanocomposites built up using magnetite and chromium oxide nanoparticles. While XRD and Raman spectroscopy prove successfully the combination of the ferrimagnetic

magnetite and the magnetoelectric antiferromagnetic chromium oxide, SQUID magnetometry demonstrates the coupling in between. These hybrid nanocomposites therefore set an example of intriguing interfacial phenomena and illustrate the importance of the interface analysis in transition metal oxide heterostructures.

Acknowledgements

J.K. is grateful for a visiting fellowship from the Institute of Advanced Study Warwick and acknowledges financial support from the Department of Physics of the University of Warwick during his sabbatical stay at Warwick. Some of the equipment used at the University of Warwick was obtained through the Science City Advanced Materials project ''Creating and Characterizing Next-Generation Advanced Materials''. The xunta de Galicia (Regional Government, Spain) had supported this work under project 10PXIB312260PR.

Notes and references

1 J. Maier, *Chem. Mater.*, 2014, **26**, 348.
2 S. Kalinin and N. A. Spaldin, *Science*, 2013, **341**, 858.
3 M. Palcut, K. Wiik and T. Grande, *J. Phys. Chem. B*, 2007, **111**, 813.
4 B. J. Beberwyck, Y. Surendranth and A. P. Alivisatos, *J. Phys. Chem. C*, 2013, **117**, 19759.
5 L. Carbone and P. D. Cozzoli, *Nano Today*, 2010, **5**, 449.
6 E. Dagotto, *Science*, 2007, **318**, 1076.
7 M. Bañobre-López, C. Vázquez, J. Rivas and M. A. López-Quintela, *Nanotechnology*, 2003, **14**, 318.
8 X. Deng, X. Li, Q. Peng, X. Wang, J. Chen and Y. Li, *Angew. Chem., Int. Ed.*, 2005, **44**, 2782.
9 J. F. Scott, *Rev. Mod. Phys.*, 1974, **46**, 83.
10 D. L. A. de Faria, S. Venancio Silva and M. T. de Oliveira, *J. Raman Spectrosc.*, 1997, **28**, 873.
11 M. N. Iliev, M. V. Abrashev, H. G. Lee, V. N. Popov, Y. Y. Sun, C. Thomsen, T. L. Meng and C. W. Chu, *J. Phys. Chem. Solids*, 1998, **59**, 1982.
12 O. N. Shebanova and P. Lazor, *J. Raman Spectrosc.*, 2003, **34**, 845.
13 J. Kreisel, M. C. Weber, N. Dix, F. Sánchez, P. A. Thomas and J. Fontcuberta, *Adv. Funct. Mater.*, 2012, **22**, 5044.
14 O. Chaix-Puchery, C. Cochard, P. Jadhav, J. Kreisel, N. Dix, F. Sánchez and J. Fontcuberta, *Appl. Phys. Lett.*, 2011, **99**, 072901.
15 H. Zheng, J. Kreisel, Y.-H. Chu, R. Ramesh and L. Salamanca-Riba, *Appl. Phys. Lett.*, 2007, **90**, 113113.
16 F. Le Marrec, R. Farhi, M. El Marssi, J. L. Dellis, M. G. Karkut and D. Ariosa, *Phys. Rev. B: Condens. Matter Mater. Phys.*, 2000, **61**, R6447.
17 T. Hart, R. Aggarwal and B. Lax, *Raman Scattering in Solids. Proc. 2nd Int. Conf. on Light Scattering in Solids*, ed. M. Balkanski, Flammarion, Paris, 1971.
18 T. Hart, S. B. Adams and H. Temkin, *Raman Scattering in Solids. Proc. 3rd Int. Conf. on Light Scattering in Solids*, ed. M. Balkanski, R. C. C. Leite and S. P. S. Porto, Wiley, New York, 1975.
19 T. Hart, H. Temkin and S. B. Adams, *Raman Scattering in Solids. Proc. 3rd Int. Conf. on Light Scattering in Solids*, ed. M. Balkanski, R. C. C. Leite and S. P. S. Porto, Wiley, New York, 1975.
20 K. F. McCarty and D. R. A. Boehme, *J. Solid State Chem.*, 1989, **79**, 19.
21 A. B. Dávila-Ibáñez, N. J. Buurma and V. Salgueiriño, *Nanoscale*, 2013, **5**, 4797.
22 S. Morup, D. E. Madsen, C. Frandsen, C. R. H. Bahl and M. F. Hansen, *J. Phys.: Condens. Matter*, 2007, **19**, 213202.
23 C. R. H. Bahl, J. Garde, K. Lefmann, T. B. S. Jensen, P.-A. Lingard, D. E. Madsen and S. Morup, *Eur. Phys. J. B*, 2008, **62**, 53.
24 R. Mariño-Fernández, S. H. Masunaga, N. Fontaíña-Troitiño, M. P. Morales, J. Rivas and V. Salgueiriño, *J. Phys. Chem. C*, 2011, **115**, 13991.
25 N. Fontaíña-Troitiño, S. Liébana-Viñas, B. Rodríguez-González, Z.-A. Li, M. Spasova, M. Farle and V. Salgueiriño, *Nano Lett.*, 2014, **14**, 640.
26 L. Néel, *C. R. Acad. Sci. Paris*, 1961, **252**, 4075.
27 N. Wu, X. He, A. L. Wysocki, U. Lanke, T. Komesu, K. D. Belashchenko, C. Binek and P. A. Dowben, *Phys. Rev. Lett.*, 2011, **106**, 087202.
28 X. He, Y. Wang, N. Wu, A. N. Caruso, E. Vescovo, K. D. Belashchenko, P. A. Dowben and C. Binek, *Nat. Mater.*, 2010, **9**, 579.
29 J. Smit and H. P. H. Wijn, *Ferrites*, Philips Technical Library, 1959.
30 S. Liébana-Viñas, R. Otero-Lorenzo, B. Rivas-Murias and V. Salgueiriño, *J. Phys.: Conf. Ser.*, 2014, **521**, 012002.
31 J. Nogués and I. K. Schuller, *J. Magn. Magn. Mater.*, 1999, **192**, 203.
32 V. Salgueiriño-Maceira, M. A. Correa-Duarte, M. Bañobre-López, M. Grzelczak, M. Farle, L. M. Liz-Marzan and J. Rivas, *Adv. Funct. Mater.*, 2008, **18**, 616.
33 L. Fallarino, A. Berger and C. Binek, *Appl. Phys. Lett.*, 2014, **104**, 022403.

